



ORIGINAL ARTICLE

In vivo monitoring an important plant immune signaling molecule salicylic acid by rhodamine-engineered probes and their density functional theory (DFT) calculations



Zi-Mian Fang, Li-Long Zhang, Jin-Jing Wang, Fang-Ze Li, Tian Wang, Hu Li*, Yan Mao, Pei-Yi Wang*

State Key Laboratory Breeding Base of Green Pesticide and Agricultural Bioengineering, Key Laboratory of Green Pesticide and Agricultural Bioengineering, Ministry of Education, Center for R&D of Fine Chemicals of Guizhou University, Guiyang 550025, China

Received 8 July 2022; accepted 27 November 2022
Available online 5 December 2022

KEYWORDS

Rhodamine probes;
Carbamate moiety;
Salicylic acid;
DFT calculations;
In vivo imaging

Abstract Monitoring the dynamic fluctuations of plant immune signaling molecules is particularly meaningful and challenging in crop protection. Herein, four rhodamine-functionalized probes (**F**₁-**F**₄) were designed and synthesized to attempt to selectively detect a plant hormone salicylic acid (SA). Screening results revealed that probe **F**₁ bearing a 4,5-dimethoxy-2-nitrobenzyl carbamate moiety was extremely sensitive and selective towards SA along with a conspicuous fluorescence “turn-on” manner. The Job’s plot experiment disclosed a 1:1 binding mode together with a binding constant of $1.34 \times 10^4 \text{ M}^{-1}$, indicating that an appreciable hydrogen bonding interaction happened between probe **F**₁ and SA, thereby leading to the spirolactam ring breakage and the succeeding fluorescence generation. Concentration-dependent titration assays offered an available linear relationship for quantifying SA (15–70 μM) and the detection limit of probe **F**₁ to SA was 1 μM . Density functional theory (DFT) calculations displayed that a smaller energy gap ($\Delta E_{\text{F1-II}} = 498.89 \text{ kJ/mol}$) was obtained between its lowest unoccupied molecular orbital (LUMO) and highest occupied molecular orbital (HOMO), manifesting that probe **F**₁ was more reactive and sensitive than those of probes **F**₂-**F**₄ ($\Delta E = 567.07 \sim 601.74 \text{ kJ/mol}$) after adsorption with salicylic acid. Meanwhile, the possible monitoring mechanism was elucidated by ¹H NMR titration experiments, probe-SA DFT calculations, and HRMS. Finally, *in vivo* confocal imaging results found that probe **F**₁ could

* Corresponding authors.

E-mail addresses: hli13@gzu.edu.cn (H. Li), pywang888@126.com (P.-Y. Wang).

Peer review under responsibility of King Saud University.



delicately and selectively monitor SA on the roots of cucumber. This study can motivate the intensive exploration of multitudinous fluorescent probes for direct SA monitoring *in vivo*.

© 2022 The Author(s). Published by Elsevier B.V. on behalf of King Saud University. This is an open access article under the CC BY-NC-ND license (<http://creativecommons.org/licenses/by-nc-nd/4.0/>).

1. Introduction

Salicylic acid (SA) is a common natural aromatic carboxylic acid that displays a multidimensional role in various fields, such as the cosmetics industry (Labib et al., 2018; Gissawong et al., 2019), medical diagnosis and prescription (Daniel et al., 2021; Li et al., 2021; Clissold et al., 1986), pesticide industry (Liu et al., 2020; Garcia-Pastor et al., 2020; Liu et al., 2021), and signal transduction events (Metraux et al., 1990; Kumar et al., 2021; Sophie et al., 2020). For instance, in medical applications, it possesses a superior efficacy for treating psoriasis, calluses, keratosis pilaris, and diabetic complications at the recommended dosage of 0.2–1.5 % (Carroll et al., 2004; Hogendoorn et al., 2018; Maghfour et al., 2020; Bouzghaya et al., 2020). Besides, SA is a prime metabolite of the common medicine aspirin (acetylsalicylic acid, ASA), which exhibits excellent antipyretic, anti-inflammatory, analgesic, and antiplatelet profiles (Li et al., 2021; Choi et al., 2015). However, abnormal levels of SA are also associated with diverse adverse effects including neurotoxicity, enhanced skin absorption, reproductive and developmental toxicity, and kidney and liver dysfunctions (Freitas et al., 2019; Davis et al., 1996; Francis et al., 1990). Therefore, it is highly imperative to develop a concise and reliable technique to timely monitor the SA levels in pharmaceutical and biological samples (Karim et al., 2006; Huang et al., 2013; Ahmad et al., 2014; Kumar et al., 2015). Similarly, in the plant kingdom, SA is a key endogenous signal molecule connected with various physiological and biochemical processes, including cellular growth, development, metabolism, and interactions with invading microorganisms (Fu et al., 2012; Jiang et al., 2015; Wang et al., 2021; Naskar et al., 2021; Han et al., 2019). In addition, numerous studies have found that SA is the essential hormone that can trigger the hypersensitive response (HR) and defensive response in plants via activating the global transcriptional and translational reprogramming to produce a network of influential pathogenesis-related species (Peter et al., 2019; Zhang et al., 2019; Park et al., 2007). Through this process, plants can acquire the miraculous systemic acquired resistance (SAR) (Vlot et al., 2021; Lim et al., 2016; Wang et al., 2005; Jones et al., 2006; Hasan et al., 2022; Hasan et al., 2021) to chronically resist the invasion of pathogenic microorganisms. Inspired by those investigations, real-time monitoring of the dynamic fluctuations of SA in plants can promote the understanding of SA-induced SAR mechanism and eventually facilitate the discovery of innovative immune activators in crop protection (Vernooij et al., 1994). Nevertheless, interfering substances from SA derivatives have strongly restricted the precise detection of SA in real samples and thereby become a particularly challenging project. Thus, a positive campaign to excavate a workable and innovative technique for monitoring SA *in vivo* is urgently required.

Fluorescent probes provide huge potentials and opportunities in bioactive species sensing and imaging in view of their superior performances, including simplicity (Hassanzadeh et al., 2019; Wang et al., 2017), low-cost (Duan et al., 2021; Wang et al., 2017; Wang et al., 2019), sensibility (Vegesna et al., 2014), selectivity (Wu et al., 2021), low detection limits (Yin et al., 2019), and real-time application (Tung et al., 2021). Currently, various fluorophores, exemplified by rhodamine, fluorescein, BODIPY, pyrene, coumarin, and naphthalimide, were elaborately decorated and employed to discriminate diverse bioactive species (Choudhury et al., 2020; Yan et al., 2017; Zhou et al., 2017; Wang et al., 2020; Wang et al., 2019; Dong et al., 2019), such as reactive oxygen/nitrogen/sulfur species, metal ions, ATP and so on (Li et al., 2014; Liu et al., 2017; Ren et al., 2021; Neupane et al., 2020; Lv et al., 2021; Yousaf et al., 2019). These fascinating researches have strongly advanced our understanding of different life phenomena and diverse

biological events, thereby inspiring us to explore innovative technologies for life regulation. More interestingly, rhodamine-based chemosensors were conspicuously pursued and developed for their broad monitoring windows, excellent sensitivity, and intriguing fluorescence “turn-on” mode in complicated subcellular microenvironments. Based on these privileged advantages, our previous studies had rationally prepared a type of five- or six-membered rhodamine probes that could selectively monitor the bioactive species, such as phytohormone, Cu^{2+} , Hg^{2+} , and H_2S *in situ* and *in vivo* (Zhao et al., 2017; Lou et al., 2017; Wang et al., 2019; Yang et al., 2020; Yang et al., 2020). To continue our research efforts on the sensing of plant-derived signal molecules for future discovery of potential immune activators, herein, four novel rhodamine-functionalized probes (**F1-F4**) bearing a carbamate moiety were designed and synthesized to attempt to selectively detect the key plant hormone salicylic acid. Within these molecular frameworks, the diacylhydrazine moiety was used to assist the formation of hydrogen bonding with SA, which would lead to the whole electron rearrangement and final ring-opening of five-membered spiro lactam substructure. Based on the above inference, rhodamine-based chemosensors possessing a conspicuous fluorescence “turn-on” manner would be developed to detect SA *in vivo*. Besides, the detection performance against various SA derivatives would be elucidated by fluorescence spectra, ^1H NMR spectroscopy, Job’s plot experiment, and density functional theory (DFT) calculations. Finally, *in vivo* monitoring of SA by fluorescence confocal imaging technique would be carried out on the roots of cucumber.

2. Materials and methods

2.1. Instruments and chemicals

All the reagents and solvents involved in the experimental process were commercially available. Distilled water was used throughout the process of spectroscopic testing. NMR spectra were performed on a JEOL-ECX 500NMR spectrometer. SEM images were captured by a Nova Nano SEM 450 instrument. DLS data were captured by DelsaNano Partice Analyzer. UV–Vis spectra were performed by a TU-1900 spectrophotometer. Fluorescence spectra were recorded on a Fluoromax-4 spectrofluorometer. Fluorescence imaging was obtained using an OLYMPUS FVMPE-RS inverted fluorescence microscope with a $25\times$ objective lens.

The various stock solutions (1.0×10^{-2} M) of SA and analogs were prepared in acetonitrile, respectively. Stock solutions of probes **F1-F4** (1.0×10^{-3} M) were prepared in acetonitrile. Test solutions of samples were prepared by following the operations: 0.1 mL probe stock solution and a certain amount of detection objects were added into a 10 mL volumetric flask; then the mixed solution is configured according to the ratio of organic solvent and water required for the test, and the mixed solution was used for the constant volume of 10 mL volumetric flask. Finally, the relevant spectra were obtained after the mixture was incubated for 3 min.

2.2. Synthesis of probe **F1**

Rhodamine B (180 mg, 0.38 mmol) and 0.4 mL phosphorus oxychloride were dissolved in 10 mL anhydrous 1,2-

dichloroethane. And then the solution was refluxed for 3 h and concentrated by evaporation under vacuum. The obtained crude acyl chloride was dissolved in 6 mL anhydrous acetonitrile, and added dropwise into the prepared intermediate 4,5-dimethoxy-2-nitrobenzyl hydrazinecarboxylate (70 mg, 0.26 mmol) in 4 mL acetonitrile solution containing 0.5 mL triethylamine, and the mixture was refluxed for 6 h. The solvent was then removed under reduced pressure to give a red oil. Finally, the crude residue was purified by silica gel column chromatography (PE:EA, 3/1) to give the probe **F₁**, a yellow solid, 124.5 mg, yield 69.4 %. ¹H NMR (400 MHz, CD₃CN) δ 7.86 (d, *J* = 7.2 Hz, 1H, benzene-H), 7.65 (d, *J* = 11.2 Hz, 1H, NO₂-benzene-H), 7.58 (dd, *J* = 12.6, 6.5 Hz, 2H, benzene-H), 7.07 (d, *J* = 15.7 Hz, 1H, benzene-H), 7.03 (s, 1H, NO₂-benzene-H), 6.47 (s, 2H, xanthene-H), 6.36 (s, 2H, xanthene-H), 6.28 (s, 2H, xanthene-H), 5.25 (s, 1H, O-CH₂), 3.92 (s, 3H, O-CH₃), 3.85 (s, 3H, O-CH₃), 3.32 (q, *J* = 6.8 Hz, 8H, *N*-CH₂CH₃), 1.09 (t, *J* = 6.9 Hz, 12H, *N*-CH₂CH₃). ¹³C NMR (101 MHz, CD₃CN) δ 155.5, 155.1, 149.6, 148.5, 134.1, 123.5, 109.6, 108.6, 108.4, 104.9, 97.9, 64.0, 56.8, 56.5, 44.6, 12.4. HRMS calc. for C₃₈H₄₂N₅O₈ 696.3028 [M + H⁺], found: 696.3018.

2.3. Synthesis of probe **F₂**

Rhodamine B (220 mg, 0.46 mmol) and 0.5 mL phosphorus oxychloride were dissolved in 15 mL anhydrous acetonitrile. Then, the solution was refluxed for 3 h and concentrated by evaporation under reduced pressure. The obtained crude acyl chloride was dissolved in 10 mL anhydrous acetonitrile, and added into the prepared carbobenzoxy chloride (44.7 mg, 0.50 mmol) solution containing 0.25 mL triethylamine dropwise, and the mixture was refluxed for 3 h. The solvent was then removed under reduced pressure to give a red oil. Finally, the crude residue was purified by silica gel column chromatography (PE:EA, 2/1) to give the probe **F₂**, a light pink solid, 190 mg, yield 80.4 %. ¹H NMR (400 MHz, CDCl₃) δ 7.96 (d, *J* = 6.9 Hz, 1H, benzene-H), 7.56–7.42 (m, 2H, benzene-H), 7.14 (d, *J* = 6.5 Hz, 1H, benzene-H), 6.55 (s, 2H, xanthene-H), 6.37 (d, *J* = 2.2 Hz, 2H, xanthene-H), 6.28 (d, *J* = 8.7 Hz, 2H, xanthene-H), 6.02 (s, 1H, CONH), 3.49 (s, 3H, O-CH₃), 3.33 (q, *J* = 7.0 Hz, 8H, *N*-CH₂CH₃), 1.16 (t, *J* = 7.0 Hz, 12H, *N*-CH₂CH₃). ¹³C NMR (101 MHz, CDCl₃) δ 153.8, 148.9, 133.4, 129.2, 128.4, 124.2, 123.5, 107.8, 104.0, 97.8, 52.8, 44.4, 29.7, 12.6. HRMS calc. for C₃₀H₃₅N₄O₄ 515.2653 [M + H⁺], found: 515.2635.

2.4. Synthesis of probe **F₃**

Rhodamine B (1 g, 2.09 mmol) was dissolved in 20 mL anhydrous ethanol, and slowly added the hydrazine hydrate (98 %, 1.2 mL, 25.05 mmol) dropwise, and the mixture was refluxed for 5 h. After cooling the above reaction mixture to room temperature, we added the dilute hydrochloric acid to adjust the pH value to 7–8. The obtained pink precipitate was filtered and dried, 0.86 g, yield 90.4 %. Then, the pink precipitate (250 mg, 0.55 mmol), 0.25 mL triethylamine and phenyl chloroformate (0.10 mg, 0.60 mmol) were mixed in 10 mL anhydrous dichloromethane. And then the solution was stirred for 7 h, and concentrated by evaporation under reduced pres-

sure. The obtained crude product was purified by silica gel column chromatography (PE:EA, 3/1) to give the probe **F₃**, a white solid, 130 mg, yield 40.2 %. ¹H NMR (400 MHz, CDCl₃) δ 7.99–7.95 (m, 1H, benzene-H), 7.53–7.44 (m, 2H, benzene-H), 7.27 (s, 2H, OCH₂-benzene-H), 7.18 (s, 3H, OCH₂-benzene-H), 7.11 (d, *J* = 6.8 Hz, 1H, benzene-H), 6.78–6.03 (m, 7H, xanthene-H & CONH), 4.97 (s, 2, O-CH₂), 3.32 (q, *J* = 6.9 Hz, 8H, *N*-CH₂CH₃), 1.15 (t, *J* = 7.0 Hz, 12H, *N*-CH₂CH₃). ¹³C NMR (101 MHz, DMSO *d*₆) δ 170.5, 164.4, 153.1, 148.4, 136.6, 133.5, 127.5, 128.4, 122.8, 107.6, 104.3, 97.0, 65.8, 59.9, 43.8, 20.9, 14.2, 12.6. HRMS calc. for C₃₆H₃₉N₄O₄ 591.2966 [M + H⁺], found: 591.2960.

2.5. Synthesis of probe **F₄**

A mixture of rhodamine B (0.250 g, 0.52 mmol), EDCI (0.130 g, 0.68 mmol), HOBt (0.091 g, 0.68 mmol), ethyl 2-hydrazinyl-2-oxoacetate (0.075 g, 0.56 mmol) and 15 mL anhydrous acetonitrile were stirred at room temperature for overnight. The solvent was then removed under reduced pressure to give a red oil. Finally, the crude residue was purified by silica gel column chromatography (PE:EA, 1/1) to give the probe **F₄**, a white solid, 83 mg, yield 28.6 %. ¹H NMR (400 MHz, CDCl₃) δ 8.16 (s, 1H, benzene-H), 7.96 (d, *J* = 6.8 Hz, 1H, benzene-H), 7.59–7.40 (m, 2H, benzene-H), 7.10 (d, *J* = 6.8 Hz, 1H, NH), 6.68 (d, *J* = 8.8 Hz, 2H, xanthene-H), 6.48–6.17 (m, 4H, xanthene-H), 4.25 (q, *J* = 7.1 Hz, 2H, O-CH₂), 3.47–3.20 (m, 8H, *N*-CH₂), 1.30 (t, *J* = 7.1 Hz, 3H, O-CH₂CH₃), 1.16 (t, *J* = 7.0 Hz, 12H, *N*-CH₂CH₃). ¹³C NMR (101 MHz, CDCl₃) δ 164.6, 159.4, 154.2, 153.5, 152.2, 149.1, 133.5, 129.0, 128.4, 128.1, 124.1, 123.6, 108.1, 103.5, 97.6, 66.2, 63.4, 44.3, 13.9, 12.6. HRMS calc. for C₃₂H₃₇N₄O₅ 557.2758 [M + H⁺], found: 557.2736.

2.6. DFT calculations of probes **F₁**–**F₄** with SA

The spin-polarized DFT computations with the local meta-GGA exchange–correlation functional M062x were carried out by using the Gaussian 16 program (Frisch et al., 2016). In this work, all geometry optimizations were fully relaxed in the acetonitrile solvation model density (SMD) (Marenich et al., 2009) model, and energy calculations were obtained with 6-31G(d) basis sets for all elements. To further refine the electronic energy, the single-point calculations were performed by using the same density functional with 6-311 + G(d, p) for main-group atoms. The bulk solvent effect of acetonitrile media was considered by the self-consistent reaction field (SCRF) method using SMD solvent model. The molecular orbitals and electrostatic distribution were visualized and analyzed by Multiwfn (Lu et al., 2012) and VMD (Humphrey et al., 1996) software.

2.7. Monitoring SA on the roots of cucumber

To test the practical application of **F₁**, *in vivo* imaging for SA was carried out using the roots of cucumber seedlings (Cucumber seeds (variety: *Cucumis sativus* Linn.) were cultured for 7 days in an incubator at 25 °C). After cucumber seedlings were cultivated in tap water for 5 days, and then were divided

into three groups. The first group was the blank control group. Cucumber roots from the second group were incubated with 30 μM **F**₁ (containing 1 % CH_3CN , v/v) for 3 h at 25 °C. Cucumber roots from the third group were incubated with 30 μM **F**₁ for 3 h and then 300 μM SA for 2 h at 25 °C. All three groups were then washed with distilled water for NIR-II imaging. The above experiments were repeated three times.

3. Results and discussion

3.1. Synthesis of rhodamine-based probes **F**₁-**F**₄

An easily synthetic approach was exploited to acquire target probes **F**₁-**F**₄ (Fig. 1). Briefly, rhodamine B was subjected to the chlorination reaction by using POCl_3 in 1,2-dichloroethane solvent to provide a crucial rhodamine chloride, which was then reacted with the corresponding 4,5-dimethoxy-2-nitrobenzyl hydrazinecarboxylate and methyl hydrazinecarboxylate under the base of triethylamine (TEA) in anhydrous CH_3CN to yield target probes **F**₁ and **F**₂, respectively. For the preparation of probe **F**₃, a key intermediate rhodamine hydrazide was initially obtained and then reacted with benzyl chloroformate under the base of TEA in dry CH_2Cl_2 . Similarly, a typical condensation reaction was occurred between rhodamine B and ethyl 2-hydrazineyl-2-oxoacetate to produce the target probe **F**₄. All the molecular structures were confirmed by NMR and HRMS analysis (Figures S1-S13). Moreover, single-crystal structures **F**₁-**F**₃ were successfully cultured and assigned to triclinic, monoclinic, and mono-

clinic crystal systems, respectively, thereby further confirming these final molecular frameworks (Fig. 2 and Table 1).

3.2. Detection performance of probe **F**₁ towards SA and SA derivatives

Upon the addition of SA to probe **F**₁ solution, a quick colour variance was occurred from the initial colorless to light red (Fig. 3a), indicating that SA could induce the ring-opening of five-membered spirolactam moiety and thereby afforded a naked-eye recognition feature. To clearly elucidate this occurrence, fluorescence spectroscopic response of probe **F**₁ to SA and SA derivatives was performed. As displayed in Fig. 3a, a strong luminescence emission at 583 nm ($I_{\text{F}_1+\text{SA}}/I_{\text{F}_1} = 72.1$ -fold enhancement, $\Phi_{\text{F}_1+\text{SA}} = 0.195$) was observed distinctly after the introduction of SA. By contrast, weak variations on the fluorescence intensity were detected by importing SA derivatives including ASA, methyl salicylate, *m*-salicylic acid, *p*-salicylic acid, salicylaldehyde, *o*-methoxybenzoic acid, *o*-methylbenzoic acid, *o*-aminobenzoic acid, catechol, and benzoic acid. This outcome was consistent with their corresponding UV-vis absorbance (Figure S14), manifesting that a highly selective colorimetric chemosensor (**F**₁) might be discovered. The Job's plot experiment disclosed a 1:1 binding mode together with a binding constant of $1.34 \times 10^4 \text{ M}^{-1}$ (Figure S15), indicating that an appreciable hydrogen bonding interaction happened between probe **F**₁ and SA, thereby leading to the spirolactam ring breakage and the succeeding fluorescence generation. Additionally, we have performed the

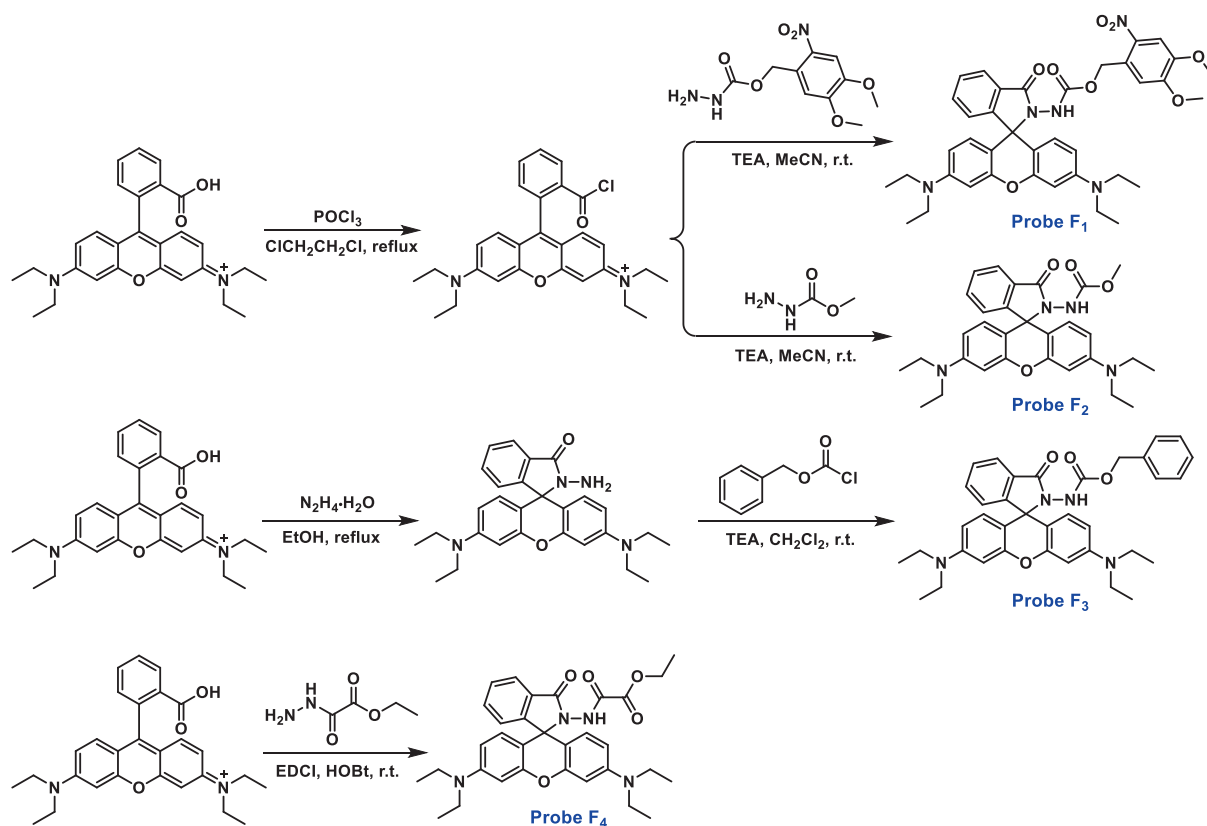


Fig. 1 Synthesis and chemical structures of rhodamine-based probes **F**₁-**F**₄.

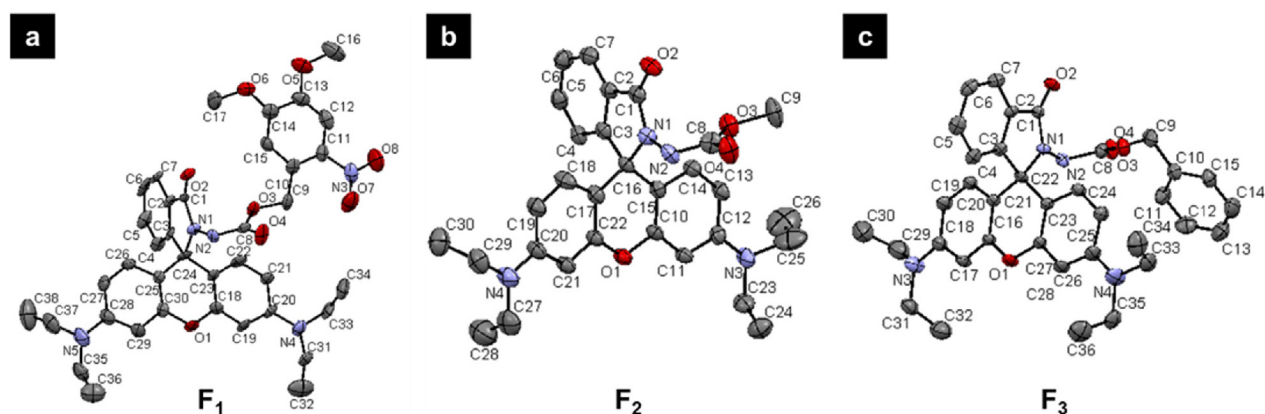


Fig. 2 Single-crystal structures of probes F_1 - F_3 .

Table 1 Crystal data and structural refinement parameters of probes F_1 - F_3 .

Compound	F_1	F_2	F_3
Formula	$C_{38}H_{41}N_5O_8$	$C_{30}H_{34}N_4O_4$	$C_{36}H_{38}N_4O_4$
CCDC numbers	2,128,774	2,128,776	2,128,779
Fw	695.76	514.62	590.72
Crystal system	Triclinic	Monoclinic	Monoclinic
Space group	$P-1$	$P2(1)/c$	$P2(1)/c$
a (Å)	9.0992(11)	9.8956(11)	9.4108(9)
b (Å)	13.0566(16)	13.1804(13)	13.3818(12)
c (Å)	14.6979(17)	24.888(3)	13.3818(12)
α (°)	83.057(3)	90.00	90.00
β (°)	83.744(3)		98.002(3)
γ (°)	77.367(2)	90.00	90.00
V (Å ³)	1685.3(3)	3192.2(6)	3405.4(5)
Z	2	4	4
Calculated density (g.cm ⁻³)	1.371	1.113	1.232
$F(000)$	736	1140	1344
Reflections	8200 / 5777	5569 / 5569	16,488 / 5979
collected/unique	[R(int) = 0.0701]	[R(int) = 0.0000]	[R(int) = 0.0918]
Goodness-of-fit on F^2	1.084	1.066	1.089
Final R indices	$R_1 = 0.1136$	$R_1 = 0.1055$	$R_1 = 0.0941$
[$I > 2\sigma(I)$]	$wR_2 = 0.2266$	$wR_2 = 0.2201$	$wR_2 = 0.2525$
R indices (all data)	$R_1 = 0.2043$, $wR_2 = 0.2591$	$R_1 = 0.2575$, $wR_2 = 0.2643$	$R_1 = 0.1896$, $wR_2 = 0.3024$

dynamic light scattering (DLS) and scanning electron microscope (SEM) experiments to check the nanoparticle of probe F_1 before and after adding SA. As shown in Figure S16, probe F_1 itself could assemble into agglomerated spherical nanoparticles with the average diameter of 388.5 nm, but having a wide size distribution from 50 to 3500 nm (Figures S16a-S16c). After adding SA into the solution of probe F_1 , spherical nanoparticles with the average diameter of 226.7 nm were observed. Moreover, these nanoparticles had a narrow size distribution from 90 to 800 nm (Figures S16d-S16f). This finding indicated that SA could trigger the ring-opening reaction of probe F_1 , and thereby afforded a new product with a planar xanthene ring and a positive charge, which would re-assemble into smaller nanoparticles with good dispersibility. To further evaluate the anti-interference performance, competitive experiments were performed by incorporating SA to

probe F_1 in the presence of various interfering substrates (Fig. 3b). Interestingly, SA analogues could not effectively trigger the ring-opening reaction of probe F_1 and led to weak fluorescent intensities at 583 nm (black bars). Whereas this situation was promptly switched after the latter supplement of the same amount of SA, thereby affording a significantly elevated fluorescence signal (red bars). This finding confirmed the excellent anti-interference ability of probe F_1 for monitoring SA in a complicated environment. Dose-dependent titration experiments disclosed that the gradual increment of SA (0–100 equivalent) could progressively elevate the fluorescence intensity of probe F_1 at 583 nm (Fig. 3c), in which an available linear relationship for quantifying SA (15–70 μ M) was deduced (Fig. 3d). The following signal-to-noise ratio measurement provided the detection limit of probe F_1 to SA was 1 μ M. Based on the above analysis, probe F_1 with good selectivity,

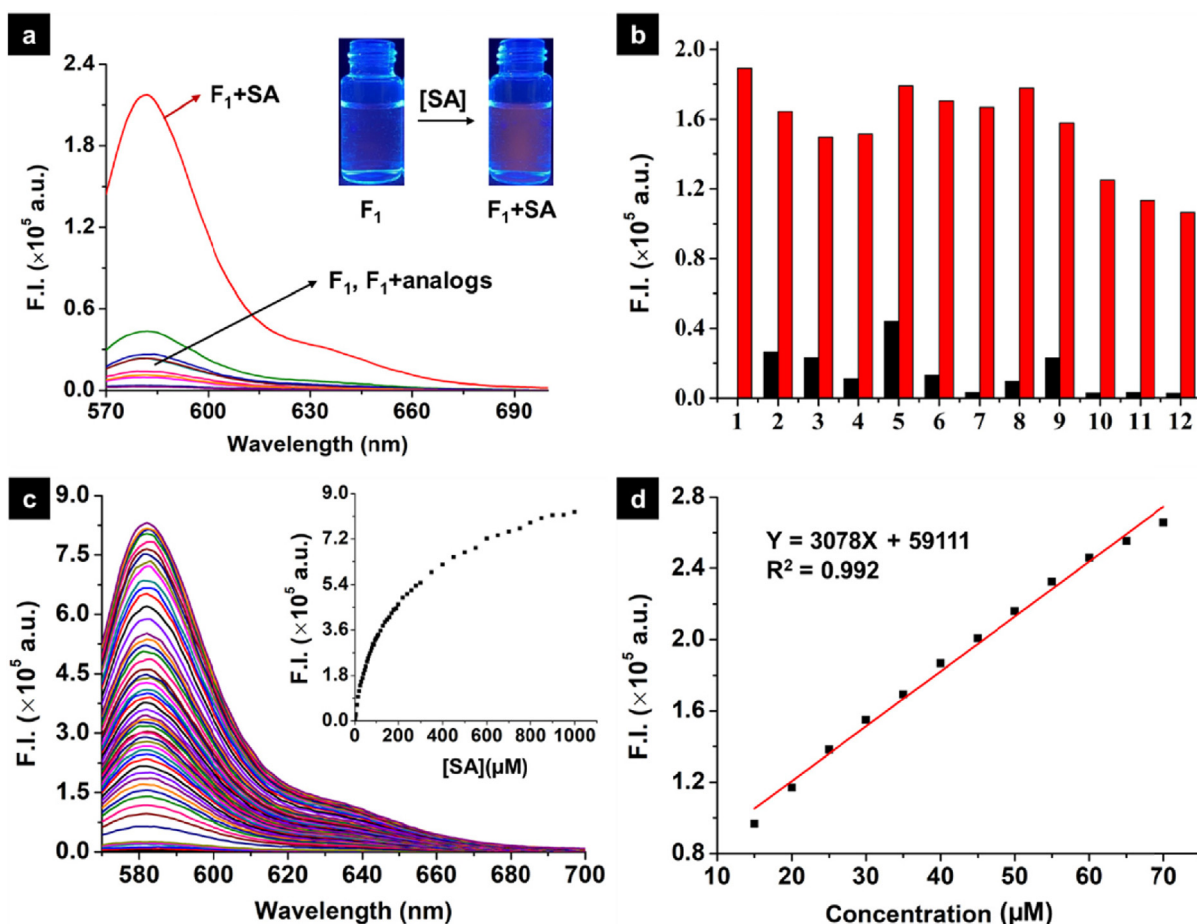


Fig. 3 (a) Fluorescence spectra of probe F_1 ($10 \mu\text{M}$) upon addition of SA and its analogs ($50 \mu\text{M}$) in the mixed solution (MeCN:H₂O = 7:3, V/V); (b) Competitive experiments for later adding $50 \mu\text{M}$ SA into premixed solutions containing probe F_1 ($10 \mu\text{M}$) and SA analogues ($50 \mu\text{M}$): (1) blank, (2) *o*-methoxybenzoic acid, (3) *m*-salicylic acid, (4) *p*-salicylic acid, (5) acetylsalicylic acid, (6) benzoic acid, (7) catechol, (8) *o*-aminobenzoic acid, (9) *o*-methylbenzoic acid, (10) phenol, (11) methyl salicylate, and (12) salicylaldehyde. Black bars, fluorescence intensity for probe F_1 and SA analogues at 583 nm; red bars, after adding SA into the premixed solution containing probe F_1 and SA analogues; (c) Fluorescence emission spectra obtained during the titration of probe F_1 ($10 \mu\text{M}$) with SA (from 0 to 1000 μM) in the mixed solution (MeCN:H₂O = 7:3, V/V). The inset shows changes in the fluorescence intensity at 583 nm; (d) The linear fluorescence (at 583 nm) change of probe F_1 ($10 \mu\text{M}$) with SA (15–70 μM). ($\lambda_{\text{ex}} = 564 \text{ nm}$, slits: 2 nm/2 nm).

sensitivity, and anti-interference competence for monitoring SA was potentially developed.

3.3. Monitoring SA by other probes F_2 - F_4 and DFT calculations for probe-SA

Structural modifications based on probe F_1 were implemented to attempt to achieve better-performance chemosensors. Therefore, probes F_2 - F_4 bearing the corresponding methyl carbamate, benzyl carbamate, and ethyl 2-amino-2-oxoacetate were prepared. The essential selectivity against SA derivatives was firstly investigated and illustrated in Fig. 4a-4c. Compared to SA derivatives, only SA could actively launch the ring-opening responses of the spiro lactam moiety of probes F_2 - F_4 , thereby causing an obvious enhancement in terms of fluorescence intensity. This finding revealed that these probes were also granted good selectivity towards SA detection. However, the sensitivity of probes F_2 - F_4 was significantly restricted by comparing to that of probe F_1 (Fig. 4d).

To disclose the reason for higher SA selectivity of F_1 , density functional theory (DFT) calculations were carried out to examine the ground state geometry of the probe molecule complex with SA as well as their corresponding binding energy and electronic structure. Our DFT calculations identified two different SA configurations, which were not distinguished in previous studies. As shown in Fig. 5 and Table S1, their geometric structures are different, and thereby attribute to striking energy differences. Given this, all analyses and calculations presented in this work are based on the most stable structure of SA.

An electrostatic potential analysis is the most useful approach to examining the relationship between structure and activity. For investigating the binding mode and energy of SA and probes (F_1 - F_4), eight possible adsorption models are predicted through two different attacking schemes (I and II). The obtained binding energy for complexes F_1 -I, F_1 -II, F_2 -I, F_2 -II, F_3 -I, F_3 -II, F_4 -I and F_4 -II were -9.65 , -12.41 , -11.02 , -11.01 , -7.76 , -11.89 , -17.49 , -8.37 kcal/mol,

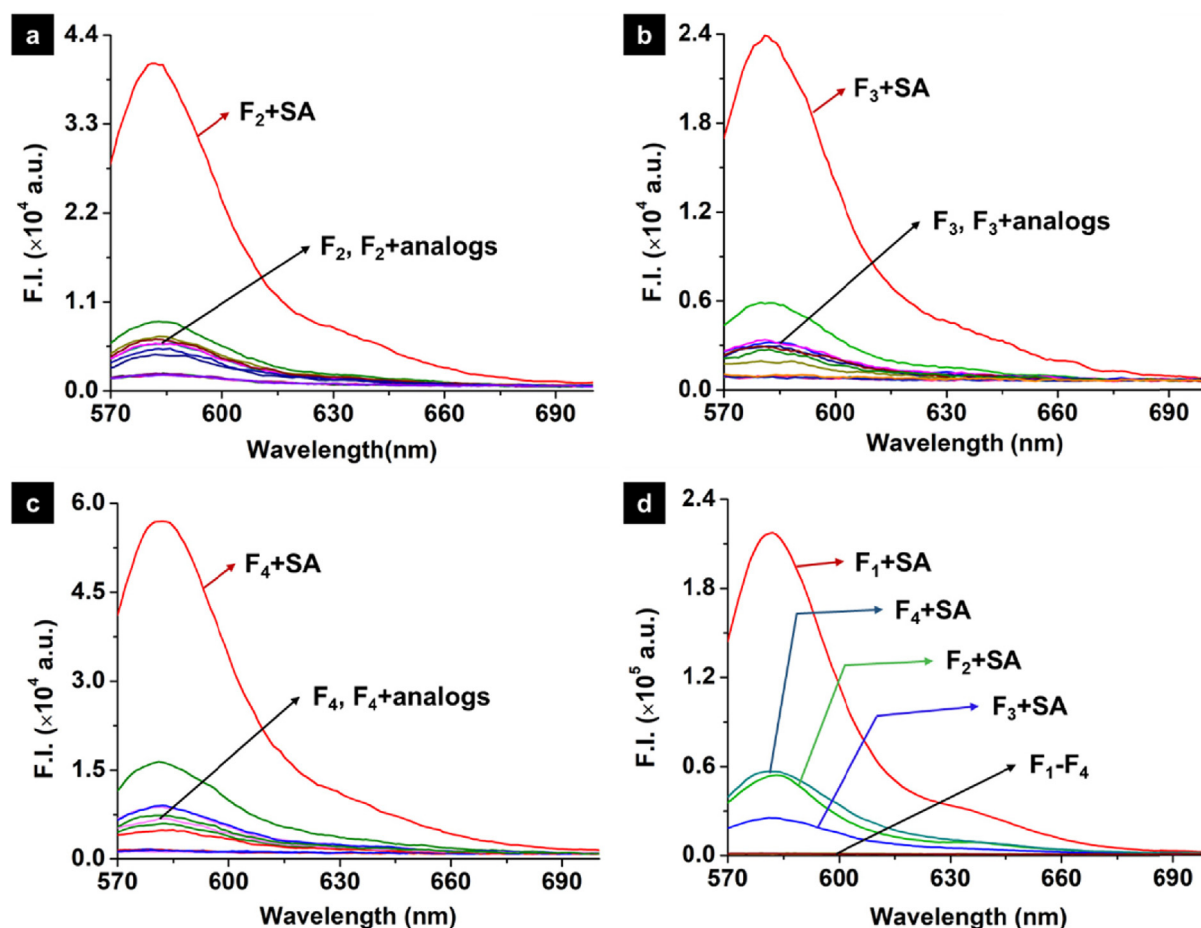


Fig. 4 Fluorescence spectra of probe F_2 (a), probe F_3 (b), probe F_4 (c) (10 μ M) upon addition of SA and its analogs (50 μ M) in the mixed solution (MeCN:H₂O = 7:3, V/V). (d) Fluorescence spectra of four Probes (10 μ M) upon addition of SA (50 μ M) in the mixed solution (λ_{ex} = 564 nm, slits: 2 nm/2 nm, MeCN:H₂O = 7:3, V/V).

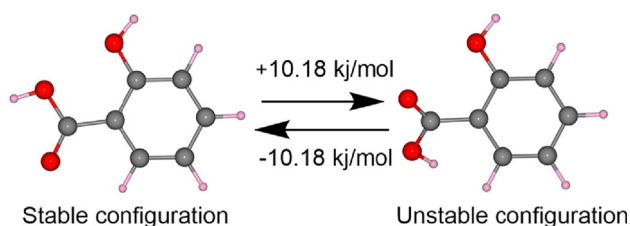


Fig. 5 Two optimized configurations of SA.

respectively (Fig. 6). Clearly, the most stable binding modes from case to case were F_1 -II, F_2 -I, F_3 -II, and F_4 -I, respectively. This finding indicates the formation of appreciable hydrogen-bonding interactions between probes and SA. The electrostatic potential penetration diagram of the most stable structures in Fig. 7a again confirms the strong hydrogen-bond interaction between SA and probe molecules. As shown in Fig. 7b, the energy gaps based on the favourable structures increase in the order: F_1 -II (498.89) < F_4 -I (567.07) < F_2 -I (591.31) < F_3 -II (601.74), suggesting that F_1 was more sensitive towards SA and could serve as a lead SA-sensor candidate for further investigations.

3.4. Possible mechanism studies for detecting SA

¹H NMR titration experiments were displayed to elucidate the possible monitoring mechanism. Upon the addition of 1.0 equivalent SA into probe F_1 solution, the proton signals (a, b, c, d) of SA shifted to the high-field region significantly ($\Delta\delta$ = -0.06, -0.05, -0.06, and -0.06 ppm, respectively, Table S2), manifesting that a strong hydrogen bonding interaction happened between the bulky probe F_1 and SA, thereby causing the increased shielding effect (Fig. 8). Inversely, continuously enhancing the amounts of SA (2.0 or 3.0 equiv.) made for the retrievable chemical shifts to low-field ($\Delta\delta$ = 0.02, 0.02, 0.03, and 0.02 ppm, respectively), indicating that a 1:1 binding mode was probably deserved, which agreed with the aforementioned Job's plot analysis. Meanwhile, the protons belonging to the isoindolinone moiety of probe F_1 gave a perceptible chemical shift to low-field via a dose-dependent manner (Table S3), exemplified by the proton at the 1-position ($\Delta\delta$ = 0.03, 0.04, and 0.05 ppm after adding 1.0, 2.0, and 3.0 equiv. SA, respectively). This phenomenon might attribute to the deshielding effect triggered by the coefficient of forming hydrogen bonds and ring-opening the spiro-lactam moiety. Nevertheless, the protons at the 4,5-dimethoxy-2-nitrobenzene ring presented a negligible chemical shift, indi-

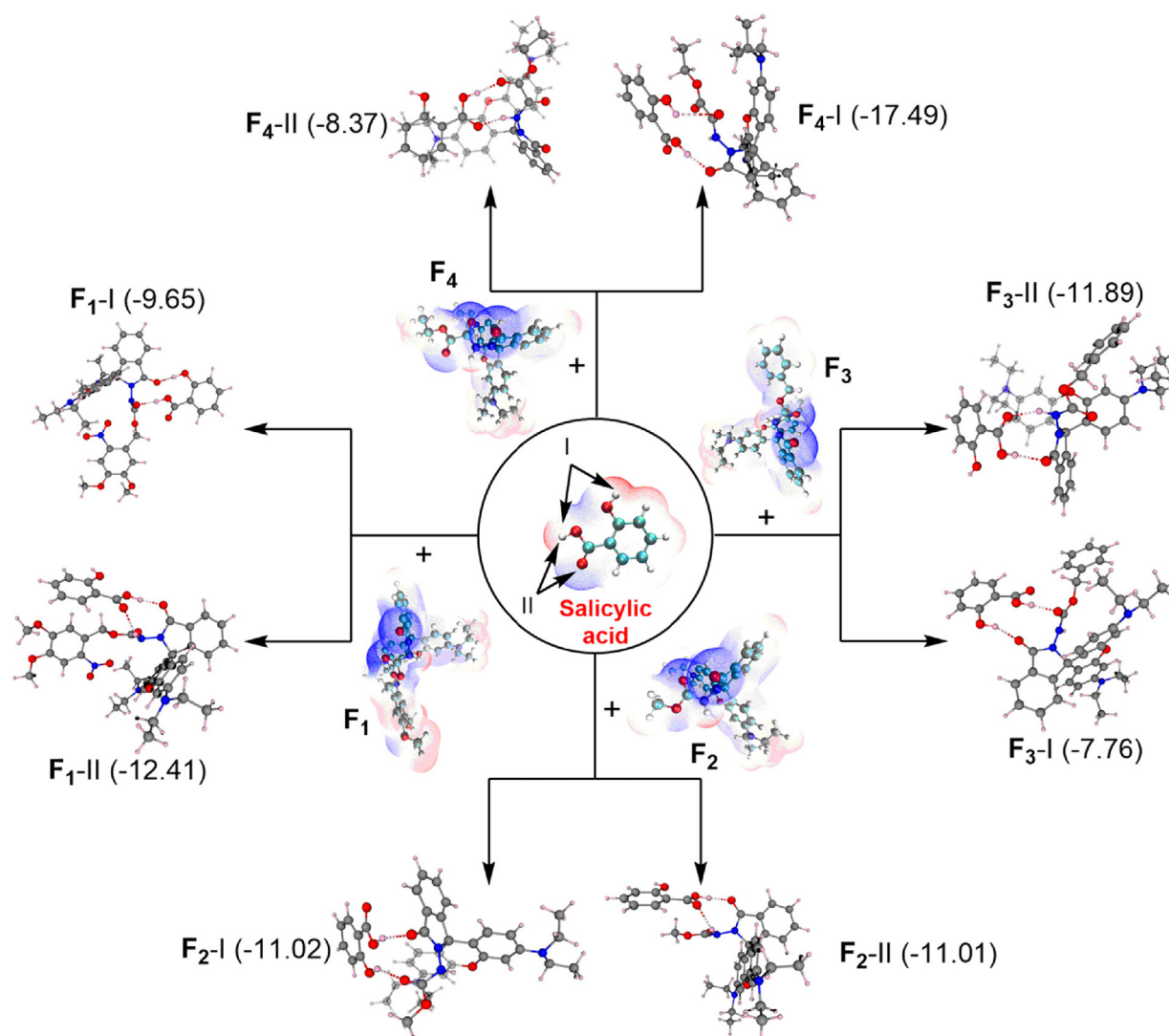


Fig. 6 The model of probes **F**₁-**F**₄ with salicylic acid.

cating that the formation of hydrogen bonds was mainly located at the carbohydrazone fragment. Notably, the chemical shift of protons (11- and 12-positions) adjacent to *N,N*-diethyl groups exhibited variations, which ascribed to the structural transformation from a closed spiroactam form to a ring-opening style and eventually facilitated the formation of quaternary ammonium. The active hydrogen (NH) of probe **F**₁ presented a large chemical shift ($\Delta\delta = 0.66$ ppm) to the low-field, further confirming that an appreciable hydrogen bonding interaction was formed with the appended SA. Given the above analysis, a possible mechanism for monitoring SA was deduced (Fig. 9). Initially, SA could participate in the formation of a relatively robust hydrogen bond with probe **F**₁, which subsequently led to the intramolecular electron migration and rearrangement. Next, this workable driving force would trigger the ring-opening reaction to yield the fluorescent-switched product for SA detection. Additionally, a molecular weight 696.3022 (*m/z*, Figure S17) for the ring-opening product from HRMS spectrum confirmed this inference.

3.5. Monitoring SA on the roots of cucumber

To evaluate the *in vivo* monitoring effect of probe **F**₁ towards SA, confocal imaging was performed on the roots of cucumber. Generally, the young roots of cucumber were incubated with 30 μ M probe **F**₁ in water for 3 h at 25 °C. After that, these roots were washed with deionized water three times and then treated with 300 μ M SA for 2 h at 25 °C. Finally, all the samples including the blank and only probe **F**₁ treatments were imaged on confocal microscopy by a two-photon excited mode. Clearly, compared to the controls (Fig. 10a-10f), the coexistence of probe **F**₁ and SA could trigger the fluorescence “turn-on” and thereby produced a strong red fluorescence located at the plant cell spaces (Fig. 10g-10i). This interesting finding revealed that probe **F**₁ could delicately and selectively monitor SA *in vivo*. Moreover, probe **F**₁ did not show potential phytotoxicity towards cucumber seedlings (Figure S18-S19 and Table S4).

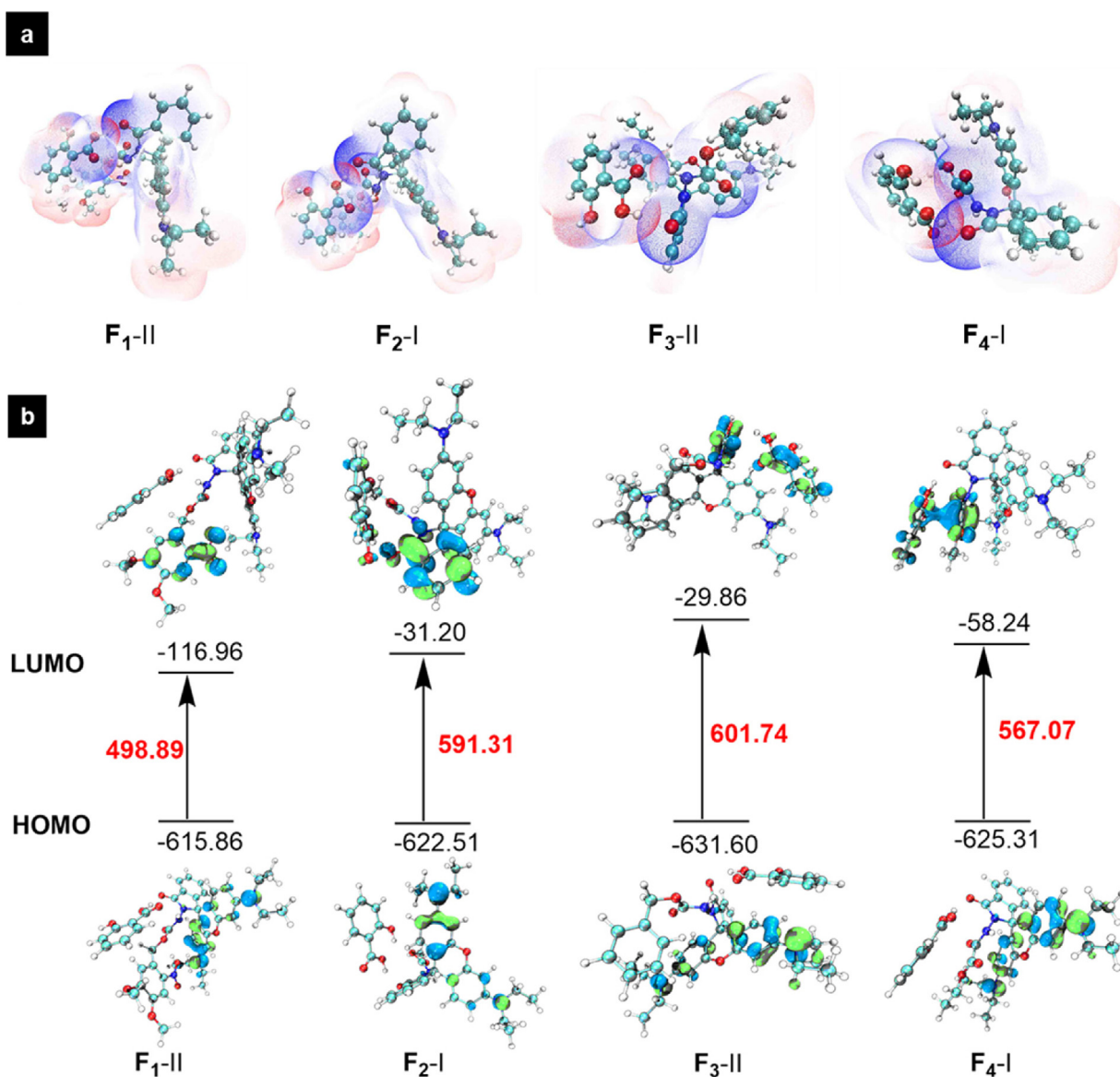


Fig. 7 (a) Electrostatic potential penetration diagram of probes **F₁-F₄** and salicylic acid; (b) HOMO–LUMO energy gap for adsorption models of probes **F₁-F₄** and salicylic acid.

In summary, four rhodamine-functionalized probes (**F₁-F₄**) bearing the carbamate moiety were prepared to attempt to selectively monitor the plant immune signaling molecule SA. Screening results displayed that probe **F₁** possessing a 4,5-dimethoxy-2-nitrobenzyl carbamate moiety could effectively and sensitively discriminate SA against various SA derivatives, which was superior to those of probes **F₂-F₄**. The following DFT calculations revealed that there was a smaller energy gap ($\Delta E_{F_1-II} = 498.89$ kJ/mol) between the LUMO and HOMO of probe **F₁**, indicating that this sensor was more reactive and sensitive than those of probes **F₂-F₄** ($\Delta E = 567.07 \sim 601.74$ kJ/mol) after adsorption with salicylic acid. ¹H NMR

titration experiments validated that a relatively robust hydrogen bonding interaction happened between probe **F₁** and SA, thereby leading to the spirolactam ring breakage and the succeeding fluorescence “turn-on”. This outcome was in agreement with the Job’s plot test, which provided a 1:1 binding mode together with an appreciable binding constant of 1.34×10^4 M⁻¹. Besides, the correlative limit of detection of 1 μM and an available linear relationship for quantifying SA (15–70 μM) were acquired (Table S5). *In vivo* imaging on the roots of cucumber further confirmed that probe **F₁** could selectively and delicately monitor SA along with producing a strong red fluorescence. Given these intriguing findings, we expected

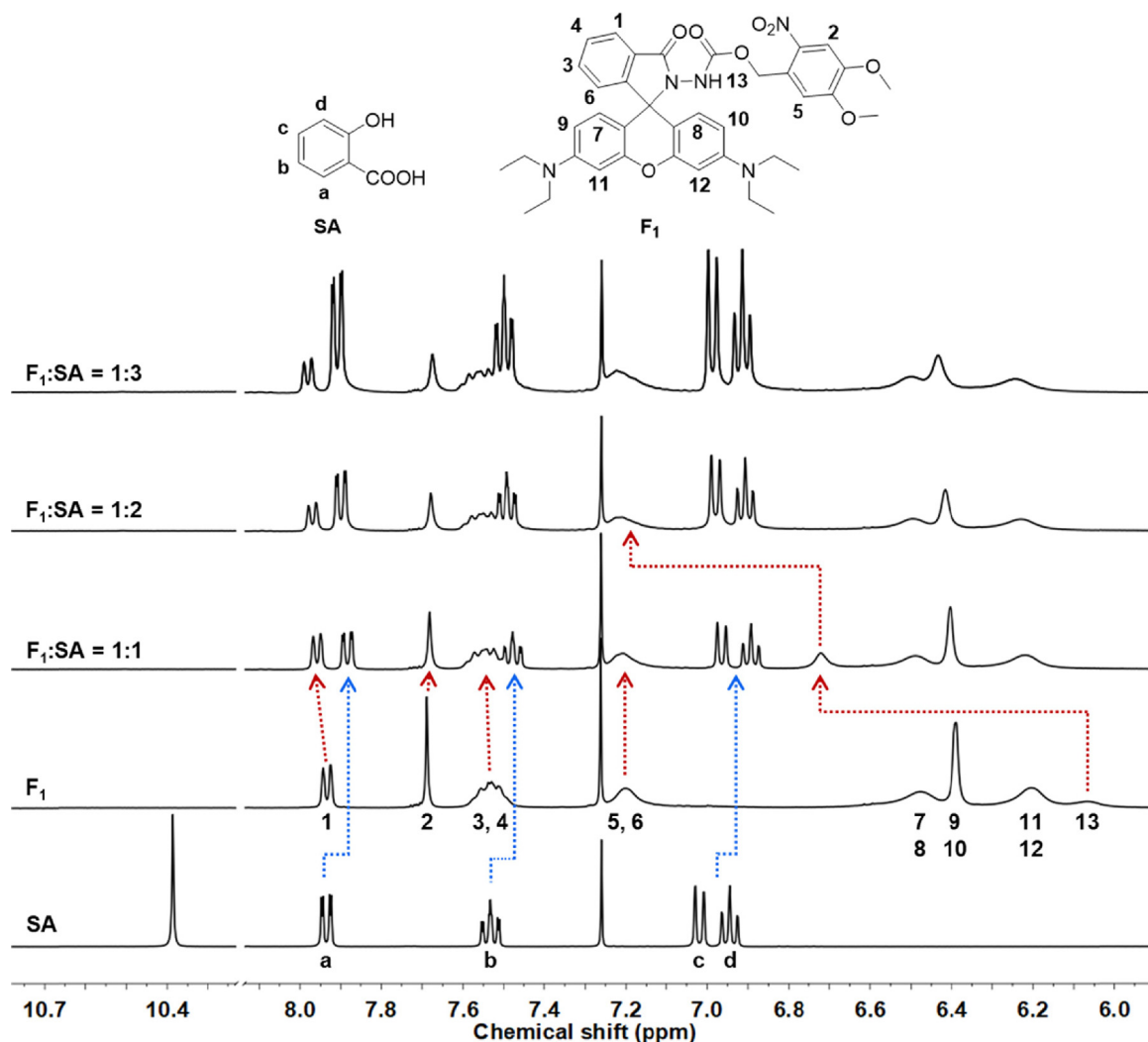


Fig. 8 Partial ^1H NMR spectra for different molar ratios of probe F_1 with SA (400 MHz, CDCl_3).

that more innovative and sensitive SA-chemosensors could be actively excavated for future research and development of plant immune activators in crop protection.

Declaration of Competing Interest

The authors declare that they have no known competing financial interests or personal relationships that could have appeared to influence the work reported in this paper.

Acknowledgment

We acknowledge funds from the National Natural Science Foundation of China, China (31860516, 21908033), Guizhou Provincial Science and Technology Project, China (ZK[2022] 017, ZK[2022]011), the high performance computing platform of Guizhou University, and the Program of Introducing Talents of Discipline to Universities of China, China (111 Program, D20023).



Fig. 9 Proposed mechanism for sensing SA using probe F_1 .

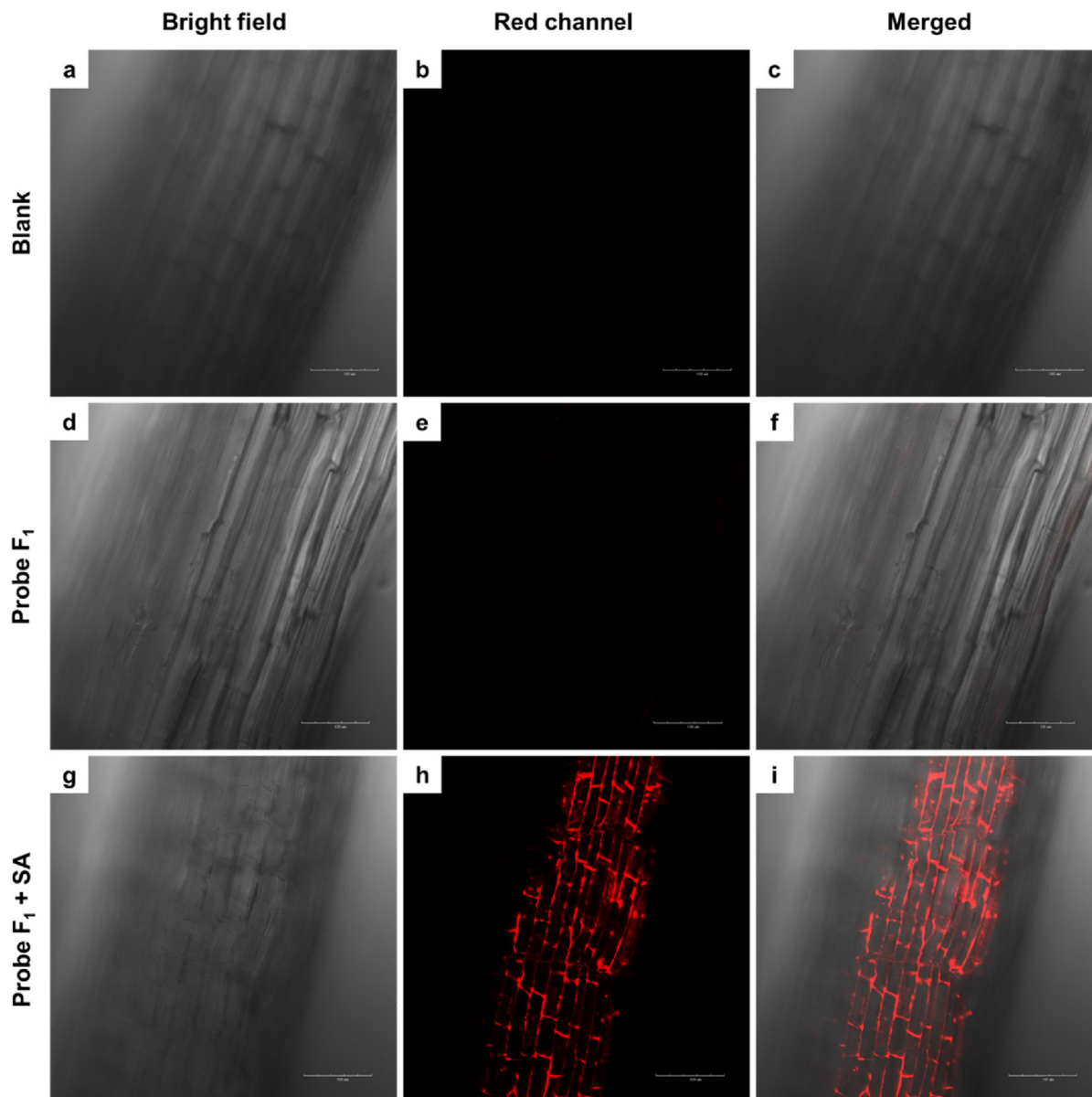


Fig. 10 Laser scanning two-photon fluorescence microscopy images of cucumber root: (a) bright-field and (b) fluorescence images of cucumber root, (c) the merged image of (a) and (b); (d) bright-field and (e) fluorescence images of cucumber root incubated with $30 \mu\text{M}$ probe F_1 for 3 h at 25°C , (f) the merged image of (d) and (e); (g) the bright-field and (h) fluorescence image of cucumber root incubated with $30 \mu\text{M}$ probe F_1 for 3 h and then $300 \mu\text{M}$ SA for 2 h at 25°C , and (i) the merged image of (g) and (h). Red channel, $\lambda_{\text{ex}} = 800 \text{ nm}$.

Appendix A. Supplementary material

Supplementary data to this article can be found online at <https://doi.org/10.1016/j.arabjc.2022.104476>.

References

- Ahmad, M.W., Kim, B.Y., Kim, H.S., 2014. Selective fluorescence sensing of salicylic acid using a simple pyrene appended imidazole receptor. *New J. Chem.* 38, 1711–1716.
- Bouzhghaya, S., Amri, M., Homble, F., 2020. Improvement of diabetes symptoms and complications by an aqueous extract of *Linum usitatissimum* (L.) seeds in alloxan-induced diabetic mice. *J. Med. Food.* 23, 1077–1082.
- Carroll, C.L., Feldman, S.R., Camacho, F.T., Balkrishnan, R., 2004. Better medication adherence results in greater improvement in severity of psoriasis. *Br. J. Dermatol.* 151, 895–897.
- Choi, H.W., Tian, M., Song, F., Venereau, E., Preti, A., Park, S.W., Hamilton, K., Swapna, G.V., Manohar, M., Moreau, M., Agresti, A., Gorzanelli, A., De Marchis, F., Wang, H., Antonyak, M., Micikas, R.J., Gentile, D.R., Cerione, R.A., Schroeder, F.C., Montelione, G.T., Bianchi, M.E., Klessig, D.F., 2015. Aspirin's active metabolite salicylic acid targets high mobility group box 1 to modulate inflammatory responses. *Mol. Med.* 21, 526–535.
- Choudhury, N., Ruidas, B., Mukhopadhyay, C.D., De, P., 2020. Rhodamine-appended polymeric probe: an efficient colorimetric and fluorometric sensing platform for Hg^{2+} in aqueous medium and living cells. *ACS Appl. Polym. Mater.* 2, 5077–5085.
- Clissold, S.P., 1986. Aspirin and related derivatives of salicylic acid. *Drugs* 32, 8–26.
- Daniel, D., Nunes, B., 2021. Evaluation of single and combined effects of two pharmaceuticals on the marine gastropod *Phorcus lineatus* enzymatic activity under two different exposure periods. *Ecotoxicology* 30, 756–765.
- Davis, D.P., Daston, G.P., Odio, M.R., York, R.G., Kraus, A.L., 1996. Maternal reproductive effects of oral salicylic acid in Sprague-Dawley rats. *Toxicol. Lett.* 84, 135–141.
- Dong, L.L., Shen, S.Q., Lu, H.Z., Jin, S.H., Zhang, J.J., 2019. Novel glycosylated naphthalimide-based activatable fluorescent probe: a tool for the assessment of hexosaminidase activity and intracellular hexosaminidase imaging. *ACS Sensors* 4, 1222–1229.
- Duan, N., Wang, H.N., Li, Y., Yang, S.X., Tian, H.Y., Sun, B.G., 2021. The research progress of organic fluorescent probe applied in food and drinking water detection. *Coordin. Chem. Rev.* 427, 213557.
- Francis, B.M., Huang, Y.S., Hartig, P.C., Rosen, M.B., Kawanishi, C. Y., Chernoff, N., 1990. Effects of murine cytomegalovirus on development: lack of interactions of virus and sodium salicylate. *J. Appl. Toxicol.* 10, 43–46.
- Freitas, R., Silvestro, S., Coppola, F., Meucci, V., Battaglia, F., Intorre, L., Soares, A., Pretti, C., Faggio, C., 2019. Biochemical and physiological responses induced in *Mytilus galloprovincialis* after a chronic exposure to salicylic acid. *Aquat. Toxicol.* 214, 105258.
- Frisch, M.J., Trucks, G.W., Schlegel, H.B., Scuseria, G.E., Robb, M. A., Cheeseman, J.R., Scalmani, G., Barone, V., Petersson, G.A., Nakatsuji, H., Li, X., Caricato, M., Marenich, A.V., Bloino, J., Janesko, B.G., Gomperts, R., Mennucci, B., Hratchian, H.P., Ortiz, J.V., Izmaylov, A.F., Sonnenberg, J.L., Williams-Young, D., Ding, F., Lipparini, F., Egidi, F., Goings, J., Peng, B., Petrone, A., Henderson, T., Ranasinghe, D., Zakrzewski, V.G., Gao, J., Rega, N., Zheng, G., Liang, W., Hada, M., Ehara, M., Toyota, K., Fukuda, R., Hasegawa, J., Ishida, M., Nakajima, T., Honda, Y., Kitao, O., Nakai, H., Vreven, T., Throssell, K., Montgomery Jr., J. A., Peralta, J.E., Ogliaro, F., Bearpark, M.J., Heyd, J.J., Brothers, E.N., Kudin, K.N., Staroverov, V.N., Keith, T.A., Kobayashi, R., Normand, J., Raghavachari, K., Rendell, A.P., Burant, J.C., Iyengar, S.S., Tomasi, J., Cossi, M., Millam, J.M., Klene, M., Adamo, C., Cammi, R., Ochterski, J.W., Martin, R.L., Morokuma, K., Farkas, O., Foresman, J.B., Fox, D.J., 2016. Gaussian 16, Revision A.03. Gaussian, Inc., Wallingford, CT.
- Fu, Z.Q., Yan, S., Saleh, A., Wang, W., Ruble, J., Oka, N., Mohan, R., Spoel, S.H., Tada, Y., Zheng, N., Dong, X., 2012. NPR3 and NPR4 are receptors for the immune signal salicylic acid in plants. *Nature* 486, 228–232.
- García-Pastor, M.E., Gimenez, M.J., Zapata, P.J., Guillen, F., Valverde, J.M., Serrano, M., Valero, D., 2020. Preharvest application of methyl salicylate, acetyl salicylic acid and salicylic acid alleviated disease caused by *Botrytis cinerea* through stimulation of antioxidant system in table grapes. *Int. J. Food. Microbiol.* 334, 108807.
- Gissawong, N., Srijaranai, S., Sansuk, S., 2019. A simple capture-release strategy based on an instantly formed mixed metal hydroxide sorbent for determination of salicylic acid in cosmetics. *Sustain. Chem. Pharm.* 13, 100154.
- Han, X., Altegoer, F., Steinchen, W., Binnebesel, L., Schuhmacher, J., Glatter, T., Giammarinaro, P.I., Djamei, A., Rensing, S.A., Reissmann, S., Kahmann, R., Bange, G., 2019. A kiwellin disarms the metabolic activity of a secreted fungal virulence factor. *Nature* 565, 650–653.
- Hasan, M., Altaf, M., Zafar, A., Hassan, S.G., Ali, Z., Mustafa, G., Munawar, T., Saif, M.S., Tariq, T., Iqbal, F., Khan, M.W., Mahmood, A., Mahmood, N., Shu, X., 2021. Bioinspired synthesis of zinc oxide nano-flowers: a surface enhanced antibacterial and harvesting efficiency. *Mat. Sci. Eng. C Mater.* 119, 111280.
- Hasan, M., Sajjad, M., Zafar, A., Hussain, R., Anjum, S.I., Zia, M., Ihsan, Z., Shu, X., 2022. Blueprinting morpho-anatomical episodes via green silver nanoparticles foliation. *Green Process Synth.* 11, 697–708.
- Hassanzadeh, J., Al Lawati, H.A.J., Al Lawati, I., 2019. Metal-organic framework loaded by rhodamine B as a novel chemiluminescence system for the paper-based analytical devices and its application for total phenolic content determination in food samples. *Anal. Chem.* 91, 10631–10639.
- Hogendoorn, G.K., Bruggink, S.C., de Koning, M.N.C., Eekhof, J.A. H., Hermans, K.E., Rissmann, R., Burggraaf, J., Wolterbeek, R., Quint, K.D., Kouwenhoven, S.T.P., Bouwes Bavinck, J.N., 2018. Morphological characteristics and human papillomavirus genotype predict the treatment response in cutaneous warts. *Brit. J. Dermatol.* 178, 253–260.
- Huang, J.X., Hu, Y.F., Hu, Y.Y., Li, G.K., 2013. Disposable terbium (III) salicylate complex imprinted membrane using solid phase surface fluorescence method for fast separation and detection of salicylic acid in pharmaceuticals and human urine. *Talanta* 107, 49–54.
- Humphrey, W., Dalke, A., Schulten, K., 1996. VMD: visual molecular dynamics. *J. Mol. Graphics.* 14, 33–38.
- Jiang, K., Kurimoto, T., Seo, E.K., Miyazaki, S., Nakajima, M., Nakamura, H., Asami, T., 2015. Development of inhibitors of salicylic acid signaling. *J. Agric. Food Chem.* 63, 7124–7133.
- Jones, J.D., Dangl, J.L., 2006. The plant immune system. *Nature* 444, 323–329.
- Karim, M.M., Lee, H.S., Kim, Y.S., Bae, H.S., Lee, S.H., 2006. Analysis of salicylic acid based on the fluorescence enhancement of the As(III)-salicylic acid system. *Anal. Chim. Acta* 576, 136–139.
- Kumar, A., Ghosh, M.K., Choi, C.H., Kim, H.S., 2015. Selective fluorescence sensing of salicylic acids using a simple pyrenesulfonamide receptor. *RSC Adv.* 5, 23613–23621.
- Kumar, J., Ramlal, A., Kumar, K., Rani, A., Mishra, V., 2021. Signaling pathways and downstream effectors of host innate immunity in plants. *Int. J. Mol. Sci.* 22, 9022.
- Labib, R., Bury, D., Boislevé, F., Eichenbaum, G., Girard, S., Naciff, J., Leal, M., Wong, J., 2018. A kinetic-based safety assessment of consumer exposure to salicylic acid from cosmetic products

- demonstrates no evidence of a health risk from developmental toxicity. *Regul. Toxicol. Pharmacol.* 94, 245–251.
- Li, Y., Cai, B.L., Zhang, Z.Y.C., Qu, G.L., Chen, L., Chen, G.J., Liang, T.X.Z., Yang, C., Fan, L., Zhang, Z.Y., 2021. Salicylic acid-based nanomedicine with self-immunomodulatory activity facilitates microRNA therapy for metabolic skeletal disorders. *Acta Bioma.* 130, 435–446.
- Li, X.H., Gao, X.H., Shi, W., Ma, H.M., 2014. Design strategies for water-soluble small molecular chromogenic and fluorogenic probes. *Chem. Rev.* 114, 590–659.
- Lim, G.H., Shine, M.B., de Lorenzo, L., Yu, K., Cui, W., Navarre, D., Hunt, A.G., Lee, J.Y., Kachroo, A., Kachroo, P., 2016. Plasmodium localizing proteins regulate transport and signaling during systemic acquired immunity in plants. *Cell Host Microbe.* 19, 541–549.
- Liu, T.T., Yuan, C.H., Gao, Y., Luo, J., Yang, S., Liu, S.K., Zhang, R.C., Zou, N., 2020. Exogenous salicylic acid mitigates the accumulation of some pesticides in cucumber seedlings under different cultivation methods. *Ecotoxicol. Environ. Safe.* 198, 110680.
- Liu, T.T., Li, T.T., Zhang, L.Y., Li, H.L., Liu, S.K., Yang, S., An, Q. S., Pan, C.P., Zou, N., 2021. Exogenous salicylic acid alleviates the accumulation of pesticides and mitigates pesticide-induced oxidative stress in cucumber plants (*Cucumis sativus* L.). *Ecotoxicol. Environ. Safe.* 208, 111654.
- Liu, J., Zhou, S.Q., Ren, J., Wu, C.L., Zhao, Y.B., 2017. A lysosome-locating and acidic pH-activatable fluorescent probe for visualizing endogenous H₂O₂ in lysosomes. *Analyst* 142, 4522–4528.
- Lu, T., Chen, F., 2012. Multiwfn: a multifunctional wavefunction analyzer. *J. Comput Chem.* 33, 580–592.
- Luo, X., He, X.D., Zhao, Y.C., Chen, C., Chen, B., Wu, Z.B., Wang, P.Y., 2017. FRET-based fluorescent and colorimetric probe for selective detection of Hg(II) and Cu(II) with dual-mode. *J. Heterocyclic Chem.* 54, 2650–2655.
- Lv, X., Han, T.H., Wu, Y., Zhang, B., Guo, W., 2021. Improving the fluorescence brightness of distyryl Bodipys by inhibiting the twisted intramolecular charge transfer excited state. *Chem. Commun.* 57, 9744–9747.
- Maghfour, J., Ly, S., Haidari, W., Taylor, S.L., Feldman, S.R., 2020. Treatment of keratosis pilaris and its variants: a systematic review. *J. Dermatolog. Treat.* 33, 1231–1242.
- Marenich, A.V., Cramer, C.J., Truhlar, D.G., 2009. Universal solvation model based on solute electron density and on a continuum model of the solvent defined by the bulk dielectric constant and atomic surface tensions. *J. Phys. Chem. B* 113, 6378–6396.
- Metraux, J.P., Signer, H., Ryals, J., Ward, E., Wyss-Benz, M., Gaudin, J., Raschdorf, K., Schmid, E., Blum, W., Inverardi, B., 1990. Increase in salicylic acid at the onset of systemic acquired resistance in cucumber. *Science* 250, 1004–1006.
- Naskar, S., Roy, C., Ghosh, S., Mukhopadhyay, A., Hazarika, L.K., Chaudhuri, R.K., Roy, S., Chakraborti, D., 2021. Elicitation of biomolecules as host defense arsenals during insect attacks on tea plants (*Camellia sinensis* (L.) Kuntze). *Appl. Microbiol. Biotechnol.* 105, 7187–7199.
- Neupane, L.N., Park, J., Mehta, P.K., Oh, E.T., Park, H.J., Lee, K.H., 2020. Fast and sensitive fluorescent detection of inorganic mercury species and methylmercury using a fluorescent probe based on the displacement reaction of arylboronic acid with the mercury species. *Chem. Commun.* 56, 2941–2944.
- Park, S.W., Kaimoyo, E., Kumar, D., Mosher, S., Klessig, D.F., 2007. Methyl salicylate is a critical mobile signal for plant systemic acquired resistance. *Science* 318, 113–116.
- Peter, B.K., 2019. The plant hypersensitive response: concepts, control and consequences. *Mol. Plant Pathol.* 20, 1163–1178.
- Ren, T.B., Wang, Z.Y., Xiang, Z., Lu, P., Lai, H.H., Yuan, L., Zhang, X.B., Tan, W.H., 2021. A general strategy for development of activatable NIR-II fluorescent probes for in vivo high-contrast bioimaging. *Angew. Chem. Int. Ed. Engl.* 60, 800–805.
- Sophie, M.B., Firuz, O., Dhar, B.D., Marit, L., Pete, E.H., Laura, G. B., Erik, A., Erland, L., Erik, A., 2020. Intact salicylic acid signalling is required for potato defence against the necrotrophic fungus *Alternaria solani*. *Plant Mol. Biol.* 104, 1–19.
- Tung, C.H., Han, M.S., Shen, Z., Gray, B.D., Pak, K.Y., Wang, J., 2021. Near-infrared fluorogenic spray for rapid tumor sensing. *ACS Sensors* 6, 3657–3666.
- Vegesna, G.K., Janjanam, J., Bi, J., Luo, F.T., Zhang, J., Olds, C., Tiwari, A., Liu, H., 2014. pH-activatable near-infrared fluorescent probes for detection of lysosomal pH inside living cells. *J. Mater. Chem. B* 2, 4500–4508.
- Vernooij, B., Friedrich, L., Morse, A., Reist, R., Kolditz-Jawhar, R., Ward, E., Uknes, S., Kessmann, H., Ryals, J., 1994. Salicylic acid is not the translocated signal responsible for inducing systemic acquired resistance but is required in signal transduction. *Plant Cell* 6, 959–965.
- Vlot, A.C., Sales, J.H., Lenk, M., Bauer, K., Brambilla, A., Sommer, A., Chen, Y., Wenig, M., Nayem, S., 2021. Systemic propagation of immunity in plants. *New Phytol.* 229, 1234–1250.
- Wang, C.Q., Dai, S.Y., Zhang, Z.L., Lao, W.Q., Wang, R.Y., Meng, X.Q., Zhou, X., 2021. Ethylene and salicylic acid synergistically accelerate leaf senescence in *Arabidopsis*. *J. Integr. Plant. Biol.* 63, 828–833.
- Wang, D., Weaver, N.D., Kesarwani, M., Dong, X., 2005. Induction of protein secretory pathway is required for systemic acquired resistance. *Science* 308, 1036–1040.
- Wang, K.P., Zhang, S.J., Lv, C.D., Shang, H.S., Jin, Z.H., Chen, S., Zhang, Q., Zhang, Y.B., Hu, Z.Q., 2017. A highly sensitive and selective turn-on fluorescent sensor for dihydrogen phosphate in living cells. *Sensor. Actuat. B-Chem.* 247, 791–796.
- Wang, K.P., Lei, Y., Zhang, S.J., Zheng, W.J., Chen, J.P., Chen, S., Zhang, Q., Zhang, Y.B., Hu, Z.Q., 2017. Fluorescent probe for Fe (III) with high selectivity and its application in living cells. *Sensor. Actuat. B-Chem.* 252, 1140–1145.
- Wang, P.Y., Luo, X., Yang, L.L., Zhao, Y.C., Dong, R., Li, Z., Yang, S., 2019. A rhodamine-based highly specific fluorescent probe for the in situ and in vivo imaging of the biological signalling molecule salicylic acid. *Chem. Commun.* 55, 7691–7694.
- Wang, X.J., Wang, X.Y., Han, Y., Li, H., Kang, Q., Wang, P.C., Zhou, F.M., 2019. Immunoassay for cardiac troponin I with fluorescent signal amplification by hydrolyzed coumarin released from a metal-organic framework. *ACS Appl. Nano Mater.* 2, 7170–7177.
- Wang, S.M., Yang, Y., Shi, X.Y., Liu, L.Y., Chang, W.X., Li, J., 2020. Multiple stimuli-responsiveness fluorescent probe derived from cyclopolymers and pyrene-ended ammonium salts. *ACS Appl. Polym. Mater.* 2, 2246–2251.
- Wang, K.P., Zheng, W.J., Lei, Y., Zhang, S.J., Zhang, Q., Chen, S., Hu, Z.Q., 2019. A thiophene-rhodamine dyad as fluorescence probe for ferric ion and its application in living cells imaging. *J. Lumin.* 208, 468–474.
- Wu, X.F., Wang, R., Qi, S.J., Kwon, N., Han, J.J., Kim, H., Li, H.D., Yu, F.B., Yoon, J., 2021. Rational design of a highly selective near-infrared two-photon fluorogenic probe for imaging orthotopic hepatocellular carcinoma chemotherapy. *Angew. Chem. Int. Ed. Engl.* 60, 15418–15425.
- Yan, F.Y., Fan, K.Q., Bai, Z.J., Zhang, R.Q., Zu, F.L., Xu, J.X., Li, X., 2017. Fluorescein applications as fluorescent probes for the detection of analytes. *TrAC Trend Anal. Chem.* 97, 15–35.
- Yang, L.L., Tang, A.L., Wang, P.Y., Yang, S., 2020a. Switching of C-C and C-N coupling/cleavage for hypersensitive detection of Cu⁽²⁺⁾ by a catalytically mediated 2-aminoimidazolyl-tailored six-membered rhodamine probe. *Org. Lett.* 22, 8234–8239.
- Yang, L.L., Zou, S.Y., Fu, Y.H., Li, W., Wen, X.P., Wang, P.Y., Wang, Z.C., Ouyang, G.P., Li, Z., Yang, S., 2020b. Highly selective and sensitive detection of biogenic defense phytohormone salicylic

- acid in living cells and plants using a novel and viable rhodamine-functionalized fluorescent probe. *J. Agric. Food Chem.* 68, 4285–4291.
- Yin, G.X., Niu, T.T., Yu, T., Gan, Y.B., Sun, X.Y., Yin, P., Chen, H. M., Zhang, Y.Y., Li, H.T., Yao, S.Z., 2019. Simultaneous visualization of endogenous homocysteine, cysteine, glutathione, and their transformation through different fluorescence channels. *Angew. Chem. Int. Ed. Engl.* 58, 4557–4561.
- Yousaf, M., Ahmad, M., Bhatti, I.A., Nasir, A., Hasan, M., Jian, X., Kalantar-Zadeh, K., Mahmood, N., 2019. In vivo and in vitro monitoring of amyloid aggregation via BSA@FGQDs multimodal probe. *ACS Sens.* 4, 200–210.
- Zhang, Y.C., Zou, Y.N., Liu, L.P., Wu, Q.S., 2019. Common mycorrhizal networks activate salicylic acid defense responses of trifoliolate orange (*Poncirus trifoliata*). *J. Integr. Plant. Biol.* 61, 1099–1111.
- Zhao, Y.C., Chen, C., Chen, B., Wang, P.Y., Wu, Z.B., Li, H., Song, B.A., Yang, S., 2017. Tunable fluorescent probes for selective detection of copper(II) and sulphide with completely different modes. *Sensor. Actuat. B-Chem.* 241, 168–173.
- Zhou, Z., Wang, F.Y., Yang, G.C., Lu, C.F., Nie, J.Q., Chen, Z.X., Ren, J., Sun, Q., Zhao, C.C., Zhu, W.H., 2017. A ratiometric fluorescent probe for monitoring leucine aminopeptidase in living cells and zebrafish model. *Anal. Chem.* 89, 11576–11582.